

Cranial function in a late Miocene *Dinocrocuta gigantea* (Mammalia: Carnivora) revealed by comparative finite element analysis

ZHIJIE JACK TSENG*

Department of Vertebrate Paleontology, Natural History Museum of Los Angeles County, 900 Exposition Boulevard, Los Angeles, CA 90007, USA

Received 19 March 2008; accepted for publication 26 April 2008

Carnivoran ecomorphologies evolved repeatedly during the Cenozoic. Whereas extreme forms (e.g. sabretoothed predators) probably represent similarities in ecology, other morphologies are more subtle with respect to the extent of their shared niche space. Finite element models of the skulls of *Dinocrocuta gigantea*, *Canis lupus*, and *Crocuta crocuta* were constructed to test the interpretation of *D. gigantea* as a bone cracker, an interpretation made on the basis of its large, conical premolars, and robust cranial morphology. *Dinocrocuta gigantea* is also of interest because it represents a lineage that has been placed in its own family, sister to Hyaenidae. Thus, functional similarity in craniodental performance could represent rapid convergence. The findings obtained indicate that the crania of *D. gigantea* and *C. crocuta* perform better in stress dissipation and distribution than that of *C. lupus*, regardless of P3 or P4 biting. In particular, the domed frontal region of the bone crackers received lower and more evenly distributed stress than *C. lupus*. Thus, the craniodental forms of the two bone-crackers are linked by functional advantage over that of *C. lupus*. Further examination of lineages such as borophagine canids could elucidate the extent of functional convergence of the bone-cracking ecomorph across diverse groups. © 2009 The Linnean Society of London, *Biological Journal of the Linnean Society*, 2009, 96, 51–67.

ADDITIONAL KEYWORDS: bone cracking – Canidae – Cenozoic – China – functional morphology – Hyaenidae.

INTRODUCTION

Our understanding of functional morphology in fossil carnivorans has been greatly augmented by studies of morphospace and ecomorphology in both extant and extinct predator guilds (Van Valkenburgh, 1988, 1989, 1999, 2001; Werdelin, 1996). General categories have been established based on correlations between craniodental form and diet in living carnivorans, and a similarity in craniodental form between living and fossil taxa. One example of an iteratively evolved mammalian carnivore ecomorphology is the bone-cracking predator, which has been characterized on the basis of craniodental morphology (Werdelin, 1989)

and enamel microstructure specialization (Rensberger, 1995; Stefen & Rensberger, 2002; Ferretti, 2007). Bone cracking carnivorans are best represented today by members of the family Hyaenidae. Although the generalizations are well established, no study has compared hyaenid craniodental forms in their response to mechanical stress imposed on the skull during bone cracking behavior. This study presents a comparative analysis of a purported fossil bone cracking carnivoran, *Dinocrocuta gigantea* Schlosser, 1903, the extant bone cracking spotted hyena *Crocuta crocuta* Erxleben, 1777, using the extant grey wolf *Canis lupus* Linnaeus, 1758 as a non-bone-cracking hypercarnivore for comparison. It is hypothesized that the craniodental morphology of *Dinocrocuta* is more suited for bone-cracking in terms of its stress-dissipating architecture because of the highly domed frontal region, than the spotted hyena.

*Current address: Integrative and Evolutionary Biology Program, Department of Biological Sciences, University of Southern California, 3616 Trousdale Parkway, Los Angeles, CA 90089-0371, USA. E-mail: jack.tseng@usc.edu

Both would perform better under loading conditions simulating bone-cracking than the grey wolf, which is a meat specialist with capability for bone-crushing with molars (for a definition of crushing versus cracking, see Werdelin, 1989) but with a very shallow forehead.

To test the functional hypothesis regarding the capability of the cranium for bone cracking, the engineering technique finite element modelling is utilized (Laitman, 2005; Richmond *et al.*, 2005; Ross, 2005). The cranial models are compared solely on craniodental form, with element volumes standardized. Because the goal of the present study is to examine the distribution and concentration of reaction forces in the cranium, stress (force per unit area) is used instead of strain (change in length relative to original length), a measure of deformation. The measure used to evaluate craniodental function in stress dissipation is the Von Mises stress, which is a scalar function incorporating principal stress in the three orthogonal planes of a three-dimensional (3D) object. Von Mises stress is also used as a criterion to evaluate how close an object is to failure (i.e. it is directly comparable to yield strength of the object; Irons & Ahmad, 1980). The expectation is that both the median Von Mises stress of the entire cranium, as well as the maximum Von Mises stress in the frontal-parietal region, hypothesized to serve an important function in stress dissipation (Buckland-Wright, 1978; Werdelin, 1989), would be lowest in *Dinocrocuta*, higher in *Crocuta*, and highest in *Canis*.

As a more recently applied methodology in the field of evolutionary biology, finite element modelling has demonstrated high potential as a tool to understand kinematics of forms (Rayfield *et al.*, 2001; Rayfield, 2004; Dumont, Piccirillo & Grosse, 2005; Laitman, 2005). The fundamental principle of this technique is to sufficiently recreate a representation analysable by computers from an extremely complex natural structure such as the skull. To build a finite element model, the basic steps include: (1) the morphology of object of interest (shape reconstruction); (2) the characteristics of the material composition of the object that governs the behavior of that object under mechanical loads (material properties); and (3) a scenario in which the object is being loaded with mechanical force, and how much force is involved (boundary conditions). Modelling of complex objects simplifies the problem at hand by making assumptions. Bone, a living and dynamic tissue, would require highly complex models to be portrayed accurately. By starting only with shape, or craniodental morphology, the present study eliminates many details of bone biomechanics (e.g. different material properties for cancellous versus cortical bone; different properties in different load directions or aniso-

tropy; bone sutures, contact between bone and tooth, etc.). However, the simplifying assumptions employed in the study means that fossils are made comparable to extant specimens by standardizing the methods of modelling. Furthermore, in any comparative analyses involving fossil material, the quality of the data is often constrained by fossil quality because many anatomical features might be incomplete or missing altogether. Assumptions made under these considerations are discussed in more detail in the model building protocol below.

The institutional abbreviations used in the present study are: IVPP, Institute of Vertebrate Paleontology and Paleoanthropology, Beijing, China; LACM: Natural History Museum of Los Angeles County (mammalogy department), Los Angeles, CA, USA; UCLA, University of California, Los Angeles, CA, USA.

MATERIAL AND METHODS

DATA ACQUISITION AND PROCESSING

An undeformed skull of *D. gigantea* (IVPP V15649) was used. Although not all fine internal structures of the bone are preserved, the specimen represents the best preserved skull of the species. The skull retains cranium and associated mandibles; the specimen comes from the late Miocene beds of Fugu, Shaanxi Province, in northern China. The associated cranium and mandibles retain a complete dentition, which is fully erupted but unworn, representing a sub-adult or young adult equivalent compared to *C. crocuta*. From the developmental stage of the cranial bones in comparison with other specimens of the same species, it was determined that this individual also does not have a fully grown cranial region. Thus, a skull of the extant spotted hyena *C. crocuta* (LACM 30655) in a similar stage of ontogenetic development was chosen for analysis and comparison. In addition, an adult grey wolf *C. lupus* (LACM 23010) skull was chosen as a hypercarnivore comparison.

All three skulls were scanned by computed tomography (CT) using a Siemens Definition 64 scanner (Siemens Medical Solutions) at UCLA Medical Center. Specimens were scanned with 0.6 mm slice thickness and a 0.6 mm interslice distance. This produced 616 images for *D. gigantea*, 464 for *C. crocuta*, and 499 for *C. lupus*. The data were then imported into the image processing software programs Amira (Visage Imaging, Inc.) and VGStudio Max (Volume Graphics GmbH), in which a combination of automated thresholding operations and manual delineation were used to identify the craniodental morphology from the image scans. For the *D. gigantea* skull, the internal cavities were filled with inorganic

matrix during burial, and the matrix has approximately the same density as the fossilized bone. Thus, manual editing of bone boundaries, visible as small gaps and fissures between fossil bone and rock matrix, was performed for all image slices. To ensure a faithful reconstruction of the fossilized bone, the slices were edited thoroughly in all three planes (axial, coronal, and sagittal). Once the regions of interest were defined, 3D representations of the crania were reconstructed.

The reconstructions were then imported into the rapid prototyping software program Geomagic Studio 9.0 (Geomagic, Inc.), which allowed operations that improved the quality and consistency of the reconstructions. The cranial reconstructions were refined, holes filled, and then decimated to 300 000 triangles, which formed the basic elements of the 3D surface reconstruction. The fossil specimen required extensive modification such as removing sharp artefacts in internal bone boundaries created during manual delineation. The mandible reconstructions were modified and cleaned separately from the cranium, but a correct orientation of articulation preserved to allow for modelling of muscle forces in the final models.

FINITE ELEMENT MODEL BUILDING

The refined reconstructions were then imported into the finite element analysis software STRAND7 (G+D Computing Pty Ltd, Sydney, Australia). In this software, the reconstruction was again checked for errors such as sharp angles between triangles and very large aspect ratios. In addition, the basic triangles of the surface reconstruction were zipped and extraneous nodes removed to create a single continuous surface. This structure was then transformed into a solid mesh of four-noded tetrahedral elements. The solid mesh reconstructions of *Dinocrocuta* and *Canis* were then standardized to that of the *C. crocuta* mesh, which had an elemental volume of 326 625 mm³. This was carried out in the STRAND7 software program by dividing the elemental volume (calculated by the software using the model summary function) of the *C. crocuta* model by the volume of the model to be standardized to get a ratio; next, the model of interest was re-scaled with the cubic-root value of this ratio in each of the *x*, *y*, and *z* axes to obtain the standardized volume. This step standardized the amount of craniodental material represented by the finite elements, and allowed differences in analytic results to be attributed to shape differences represented by the cranial models. This approach is appropriate for the hypothesis being tested because, once the amount of craniodental material present in all three cranial models is standardized, the analyses

could address how remaining morphological differences such as frontal shape and thickness affect the stress-dissipating function of the structures during unilateral premolar biting.

After a reconstruction of the original morphology was achieved, the solid mesh needed to be assigned (1) material properties and (2) boundary conditions (constraints and loads). Although voxel-based techniques are now able to import density differences (as Hounsfield units) in CT data directly into the final model for assigning multiple material properties (McHenry *et al.*, 2007), this was simply not practical for more typical fossil specimens. For most fossil skulls, including the *D. gigantea* investigated in the present study, many minute details of the cranium have been obliterated by diagenesis, and cavities are often filled by different minerals. These modifications are amplified in the scanning process and localized diagenesis can create density differences in the CT data even along small distances of a single bone. Thus, a direct import of the density data from CT scans does not create a correct representation for such specimens. To enable direct comparison with extant skulls, the craniodental reconstruction was assumed to represent a homogeneous, isotropic, elastoplastic material. For static analyses, the only required material properties under this assumption are Young's modulus (*E*) and Poisson's ratio (*v*).

The range of Young's modulus values provided in Erickson, Catanese & Keaveny (2002) for birds and mammals is in the range 15–30 GPa, and finite element models used in this study were run with this range of values at 5-GPa intervals. All returned similar results, but only data using *E* = 20 GPa (i.e. the mean for birds and mammals; Erickson *et al.* (2002): table 1) are presented here. Given the variation in Poisson's ratio depending on state of fatigue of the test specimen (Pidaparti & Vogt, 2002) and the large range of values (from 0.1 to over 0.5) published for both cranial and post-cranial bones of mammals (Reilly & Burstein, 1975; Peterson & Dechow, 2003; Peterson, Wang & Dechow, 2006; Wang, Strait & Dechow, 2006; Shahar *et al.*, 2007), a range of Poisson's ratio values were tested. When the same models were run using *v* = 0.1 to 0.5 in 0.1 intervals, the median Von Mises stress values decreased between 1% and 4% for every 0.1 increase in *v* (data not shown). A sensitivity study is currently in progress to further quantify the effect of changing *v* values on model outcomes. All data presented here used a mid-range Poisson's ratio of 0.3. Because the data are interpreted comparatively, the conclusions made here are not likely to be altered by slight changes in the exact Poisson's ratio used. All three models were assigned identical material properties. Using an estimated density of 2 mg mm⁻³ for dog cortical

bone (Cowin, 1989), together with standardized bone volumes, the final models had a skull mass close to 653.25 g (see Appendix, Table A1). Model skull mass exceeds the actual dry skull mass by 137% in *C. crocuta* and by 193% in *C. lupus*. This difference imparts additional strength in the skull models by treating all skull bone (and teeth) as cortical bone; therefore, the absolute stress values obtained in the analyses are probably lower than would be present in actual skulls.

The boundary conditions included constraints at three locations on the cranial models: (1) left temporomandibular joint; (2) right temporomandibular joint; and (3) tooth of interest. The temporomandibular joints were fixed from any movement by ten arbitrary fixed nodes on each joint, approximately representing the length of contact between the glenoid and the mandibular articular processes. In addition, the tip of the tooth of interest (e.g. P3 for bone-cracking) was fully constrained from movement. The main cusp of P3, paracone of P4, and paracone and metacone of M1 were constrained in the respective models. These boundary conditions are meant to represent the simulation of an instantaneous linear static load applied to a food item (i.e. bone) at the moment of peak force applied through the tooth of interest by actions of the temporalis and masseter muscles.

Finally, the loads applied to the models were the contracted muscles of the temporalis and masseter on both sides of the cranium. The pterygoid muscles were not modelled because empirical data are lacking for extant carnivorans, and thus introducing estimated forces would only increase uncertainty in these models, in particular for *Dinocrocuta*. The muscle forces were simulated by creating thin plates over the area of bone where the respective muscles originate. The insertion sites of the temporalis and masseter were identified by bone rugosities where muscles attach on the mandibles and from muscle dissection of an extant specimen of *Hyaena hyaena* (LACM freezer catalogue number 42206) conducted at the LACM. The software program BONELOAD (Grosse *et al.*, 2007) was used to create tangentially oriented forces on the cranium, simulating the wrapping of the muscles around the cranium (Fig. 1). The insertion directions of those two masticatory muscles on the mandibles were pointed toward the center of the ascending ramus for temporalis, and at the midpoint of the lateral ridge ventral of the mandibular fossa that extends posteriorly to the angular process for masseter, respectively. This method simulates the approximate pulling direction of the contracting musculature, but does not account for differences in muscle fiber angles that might exist between groups within each muscle.

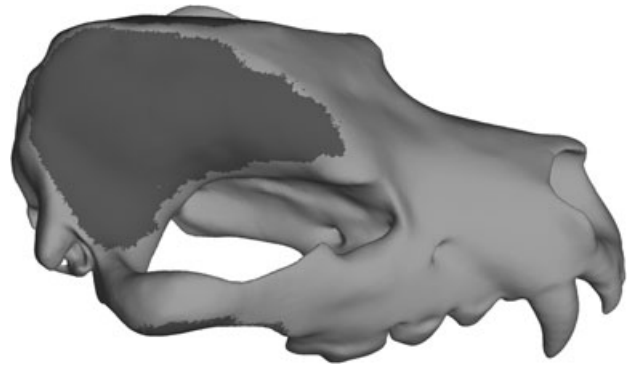


Figure 1. Finite element model of *Dinocrocuta gigantea* with muscle insertion areas of the temporalis and masseter created (dark grey areas) using the BONELOAD program (Grosse *et al.*, 2007). Anterior dorsolateral view. The length of the cranium is approximately 322 mm. Other models were constructed similarly by demarcating regions of temporalis and masseter attachment. Mandibles were included for identification of resultant muscle force directions, and then removed before analyses were run.

As all three models were scaled to approximately the same element volume, that of *C. crocuta*, and the specimen of *Crocuta* used represents a sub-adult with fully erupted permanent dentition but with still developing cranial bones, a bite force of 318.15 N at the P4 was used in all analyses. This bite force was derived from the regression equation of empirical bite force data taken by Binder & Van Valkenburgh (2000) calculated for a 12-month-old captive spotted hyena:

$$\text{Bite force} = 165.952 + 12.683 \times \text{age}$$

Each model was loaded with an arbitrary 1000 N total muscle force, with the proportions of muscle activation set as described above. Because bite force measurements were taken with a fork force transducer by Binder & Van Valkenburgh (2000), which converts vertical displacement of the forks to change in detected current, the resulting values represent force perpendicular to the plane of occlusion. Thus, the resulting bite force produced at the cusp tip of P4 paracone, perpendicular to the tooth occlusal plane, was analysed. The new resultant total muscle force was calculated as below (Dumont *et al.*, 2005), and then distributed according to the muscle activation scheme:

$$(F_t)_{\text{new}} = (F_{\text{exp}}/F_{\text{R}}^N) \times F_t$$

where $(F_t)_{\text{new}}$ is the resultant muscle force required to produce F_{exp} ; F_{exp} is the experimentally measured force, in this case 318.15 N from Binder & Van Valkenburgh (2000); and F_{R}^N is the resulting bite force from the initial arbitrarily chosen total muscle force, F_t .

The relative proportions of muscle activation between the temporalis and masseter, and between the working and balancing side muscles in unilateral biting, can affect the model results. In all the models constructed, a 60% difference between the balancing side and working side muscle activation was used. This value is based on Dessem's (1989) empirical data for domestic dog, which showed that, during unilateral bone-crushing with M1, the balancing side muscles acted at 60% of the maximum recorded electromyographic activity. Although quantitative data have been collected on muscle recruitment in cats (Gorniak & Gans, 1980), the Dessem study included M1 bone-crushing behavior, under which loading condition better approximates bone-cracking than one feeding on soft tissue only (as in the cat study). Thus, the total required muscle force to produce a bite force of 318.15 N was distributed with the balancing side muscle force being 60% of working side muscle force. Next, the division of forces between the temporalis and masseter muscles on each side was made proportional to the estimated cross-sectional areas of the respective muscles, using the photography protocol outlined in the dry skull method (Thomason, 1991; Wroe, McHenry & Thomason, 2005). Photos of dorsal and ventral cranium were taken perpendicular to the plane of muscle cross-section as in Thomason (1991), and the area of the plane measured using IMAGEJ (Rasband, 1997–2007). A summary of the muscle force values used in the analysis is provided in the Appendix (Table A1).

DATA ANALYSIS

The biting scenarios examined were: (1) unilateral P3 biting, simulating a bone-cracking bite; (2) unilateral P4 biting, simulating a shearing bite for all three models; and (3) unilateral M1 biting, simulating a crushing molar bite in the wolf *C. lupus*. All scenarios were analysed for both left and right unilateral biting to identify any asymmetric biases. In addition, the muscle forces derived from the P4 bite force calculation were used to model both P3 and M1 biting. Three types of data were collected from the models for each biting scenario: (1) scaled median Von Mises stress of tetrahedral elements in the entire cranium, and their respective deviations; (2) scaled median and maximum Von Mises stress of tetrahedral elements in the frontal-parietal region ('frontal dome') where morphological changes have been hypothesized to represent functional adaptation; and (3) change in raw Von Mises stress of tetrahedral elements along the sagittal plane of the frontal dome, representing changes in stress as it is dissipated from the originating tooth to the rest of the cranium.

For the same amount of stress and volume, the models having larger number of tetrahedral elements

will have lower raw stress per element. Therefore, the contribution of each element to the overall stress should be made proportional before comparisons are made. Scaled median stresses were calculated after multiplying the tetrahedral element stress results by their respective volumes and then dividing by the median tetrahedral volume (i.e. to eliminate the effect of high stress simply from isolated small elements in the solid mesh, thus leaving high stress correlated with model shape). The scaled values were approximately linear to tetrahedral volume after transformation; thus, differences between models can be attributed to morphological difference in the models.

Because stress distribution in the models was expected to be highly skewed, with most of the elements under little stress, and a few elements sustaining high stress, the descriptive statistics employed include the median, standard error (SE) of the median, median absolute deviation (MAD) from the median, and interquartile range (IQR). All of the above statistics are robust measures, which are insensitive to outliers caused by model singularities and sharp features; at the same time, these descriptive measures are sufficient in using the entire dataset. Because of variation in model quality across different specimens as well as fossil versus extant taxa, another robust measure of central tendency, the trimmed mean (summing average of dataset by trimming a set percentage from the ends of the data), was not used. The reason is difficulty in objectively delineating singularities versus 'real' data consistently in all three models. All statistical summaries were calculated in the software program JMP IN (SAS Institute).

For mid-sagittal plane point sampling, data were collected in each of seven mid-sagittal landmarks. Moving posteriorly, stresses from single nodes were sampled from the mid-sagittal point at the position of: (1) the mid-sagittal anterior edge of nasal bones; (2) the central point of the infraorbital foramen; (3) the most anterior point of the orbits; (4) the tip of the post-orbital processes; (5) the point of maximal post-orbital restriction of the frontal-parietal region; (6) the anterior-most point of the sagittal crest; and (7) the posterior-most point of the sagittal crest. The single nodes recorded stress at these specific landmarks; each was sampled five times. In addition, mean stresses for ten nodes within a circular area around each landmark, covering approximately 6 mm in diameter, were sampled.

RESULTS

WITHIN-MODEL COMPARISONS

For *Canis lupus*, no consistent stress pattern could be discerned from values measured on the entire cranium

for the different biting scenarios (Table 1). Furthermore, left and right biting with the same tooth position vary only slightly. P3 biting appears to result in higher scaled median stress compared to P4 biting, but not M1. The dispersion of stress values is comparable across all scenarios as described by the MAD and IQR. The results from the frontal dome, however, show that the scaled median stresses for all biting scenarios are at least doubled from the recorded values for the entire cranium. In addition, the dispersion of stress values also increases in the frontal region. The maximum stress is comparable for all biting scenarios. IQR increases slightly for scaled stress in the frontal region. In the *Dinocrocuta* model, all stress measures are comparable across biting scenarios for the entire cranium (Table 2). Only small differences were found between left and right sides. The scaled median stress increases slightly for the frontal dome. IQR decreases from the entire cranium to the frontal region in all cases. Both the scaled and absolute maximum stresses are comparable across all scenarios. The median scaled stress of the entire cranium has an overlapping range between P3 and P4 analyses in the *Crocuta* model (Table 3). By comparison, the frontal dome has a slightly increased median stress. The maximum stress in the inter-orbital region is comparable for P3 and P4 biting. The IQR of scaled median stress increases slightly for the frontal region for all scenarios except left P4 biting. Only slight differences were found between left and right sides.

BETWEEN-MODEL COMPARISONS

For the entire cranium, median raw stress is highest in *Canis* and comparable in the other two models for P3 and P4 biting (Figs 2, 3). Scaled median stress of P4 biting is similar in *Dinocrocuta* and *Canis*, but higher during P3 biting for *Canis* (Tables 4, 5). *Crocuta* had the lowest scaled median stress values for all biting scenarios. The dispersion of stress values (MAD, IQR) of raw stress is highest in *Canis* and lowest in *Crocuta*; however, the scaled stress dispersion is comparable between *Dinocrocuta* and *Canis*, and somewhat lower in *Crocuta*. For the frontal dome, both raw and scale median stress are lowest overall in *Dinocrocuta*; in the *Canis* model, the raw and scaled median stress increased by 50% or more over those of the *Dinocrocuta* and *Crocuta* models. The same trend is observed for both raw and scaled measures of dispersion (MAD, IQR). The raw maximum stress of *Crocuta* frontal dome is approximately three times of that in *Dinocrocuta*, and that of *Canis* is approximately five times as much as in *Dinocrocuta*. The scaled maximum stress is highest in *Crocuta*, and lowest in *Dinocrocuta*. The highest overall scaled maximum stress in *Crocuta* is during left P3 biting,

Table 1. Descriptive statistics of Von Mises stress in the *Canis lupus* finite element model

	IP3	rP3	IP4	rP4	IM1	rM1
Entire model						
Median scaled \pm SE (MPa)	0.5440 \pm 0.0019	0.5061 \pm 0.0018	0.4872 \pm 0.0017	0.4257 \pm 0.0015	0.5203 \pm 0.0019	0.4447 \pm 0.0017
Scaled MAD (MPa)	0.45	0.42	0.41	0.36	0.44	0.38
Scaled IQR (MPa)	1.28	1.20	1.17	1.01	1.26	1.12
Frontal dome						
Median scaled \pm SE (MPa)	1.2075 \pm 0.0220	1.0956 \pm 0.0194	1.1824 \pm 0.0228	0.8423 \pm 0.0155	1.2435 \pm 0.0245	1.1508 \pm 0.0222
Scaled MAD (MPa)	0.78	0.68	0.77	0.53	0.82	0.74
Scaled IQR (MPa)	1.79	1.58	1.86	1.26	2.00	1.81
Maximum scaled (MPa)	18.33	19.41	20.45	16.07	21.49	23.02

Data shown are for both the entire cranium as well as the frontal region. Scenarios tested include third premolar (P3), fourth premolar (P4), and first molar (M1) biting. Both right and left side unilateral loading cases were analysed. IQR, interquartile range; MAD, median absolute deviation from the median; MPa, megapascal; SE, standard error of the median. For a definition of the terms, see text.

Table 2. Descriptive statistics of Von Mises stress in the *Dinocrocuta gigantea* finite element model

	IP3	rP3	IP4	rP4
Entire model				
Median scaled \pm SE (MPa)	0.4715 \pm 0.0016	0.4813 \pm 0.0015	0.4519 \pm 0.0015	0.5108 \pm 0.0016
Scaled MAD (MPa)	0.41	0.41	0.39	0.44
Scaled IQR (MPa)	1.24	1.20	1.17	1.28
Frontal dome				
Median scaled \pm SE (MPa)	0.7033 \pm 0.0154	0.6576 \pm 0.0140	0.6141 \pm 0.0133	0.5904 \pm 0.0136
Scaled MAD (MPa)	0.50	0.46	0.43	0.44
Scaled IQR (MPa)	1.18	1.07	1.02	1.04
Maximum scaled (MPa)	6.27	5.63	6.74	6.23

Data shown are for both the entire cranium as well as the frontal region. Scenarios tested include third premolar (P3) and fourth premolar (P4) biting. Both right and left side unilateral loading cases were analysed. Abbreviations are as shown in Table 1. For a definition of the terms, see text.

Table 3. Descriptive statistics of Von Mises stress in the *Crocuta crocuta* finite element model

	IP3	rP3	IP4	rP4
Entire model				
Median scaled \pm SE (MPa)	0.4074 \pm 0.0019	0.3333 \pm 0.0017	0.3951 \pm 0.0018	0.3704 \pm 0.0017
Scaled MAD (MPa)	0.35	0.29	0.33	0.31
Scaled IQR (MPa)	1.21	1.06	1.11	1.09
Frontal dome				
Median scaled \pm SE (MPa)	0.6950 \pm 0.0132	0.5862 \pm 0.0118	0.6083 \pm 0.0113	0.5769 \pm 0.0116
Scaled MAD (MPa)	0.48	0.42	0.41	0.40
Scaled IQR (MPa)	1.25	1.12	1.07	1.10
Maximum scaled (MPa)	57.77	40.44	52.76	48.68

Data shown are for both the entire cranium as well as the frontal region. Scenarios tested include third premolar (P3) and fourth premolar (P4) biting. Both right and left side unilateral loading cases were analysed. Abbreviations are as shown in Table 1. For a definition of the terms, see text.

and it is close to ten times the scaled stress in *Dinocrocuta*.

POINT SAMPLING ALONG MID-SAGITTAL PLANE OF DORSAL CRANIUM

Seven points were chosen to document the change in absolute stress along the mid-sagittal plane, including the frontal region which is highly domed in *Dinocrocuta* (Fig. 1). All five samples returned similar stress trends; one representative trend from each biting scenario is presented in Figure 4A, B, C. In the *Crocuta* model, P3 biting creates peak stress in the region between anterior borders of the orbits, whereas P4 biting peaks between the post-orbital processes (Fig. 4A). In *Dinocrocuta*, the pattern is the same as in *Crocuta*; the only difference is that the first peak at the anterior orbit boundary is not as pronounced relative to the inter-orbital region of the post-orbital processes as in *Crocuta* (Fig. 4B). In *Canis*, two peaks

are present in P3 biting: one between the infraorbital foramina, the other at the anterior tip of the sagittal crest (Fig. 4C). For P4 biting, there are also two peaks, but the first one has shifted from infraorbital foramina to inter-orbital region between post-orbital processes. M1 biting shows a similar pattern as the P4 data for *Canis*. When the mean stresses along the identical landmarks are sampled across a circular area of ten nodes, the same patterns are observed in *Crocuta* and *Dinocrocuta* (Fig. 4D, E). However, in *Canis*, the stress peaks previously observed around the infraorbital foramina and the anterior tip of the sagittal crest became less obvious in the mean sample, but P3 biting still exhibits more abrupt stress increases in those regions (Fig. 4F).

DISCUSSION

All within-model results demonstrate that, given the same muscle force input, P3 and P4 biting generate

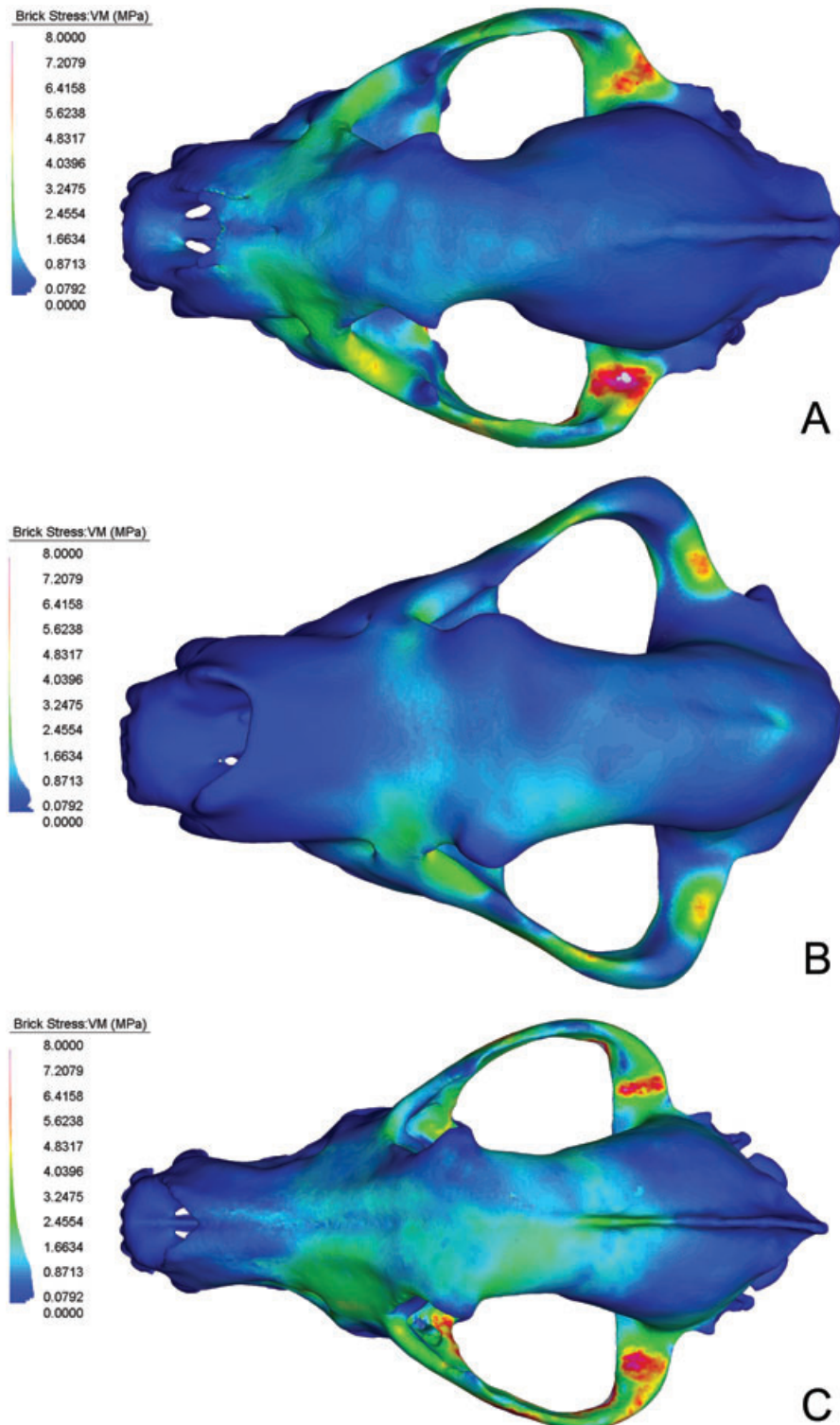


Figure 2. Dorsal views of Von Mises (VM) stress distribution during left P3-biting scenario in the cranium of (A) *Crocuta crocuta*, (B) *Dinocrocuta gigantea*, and (C) *Canis lupus*. All legends are scaled to have a range of 0–8 MPa for optimized visualization. The deeper blue areas represent small or no stress and the red areas represent highly stressed regions. White patches represent areas where stress exceeds 8 MPa. The crania are scaled to approximately the same length in the figure. Right P3 biting and right and left P4 biting scenarios produced similar stress distributions that are not statistically different.

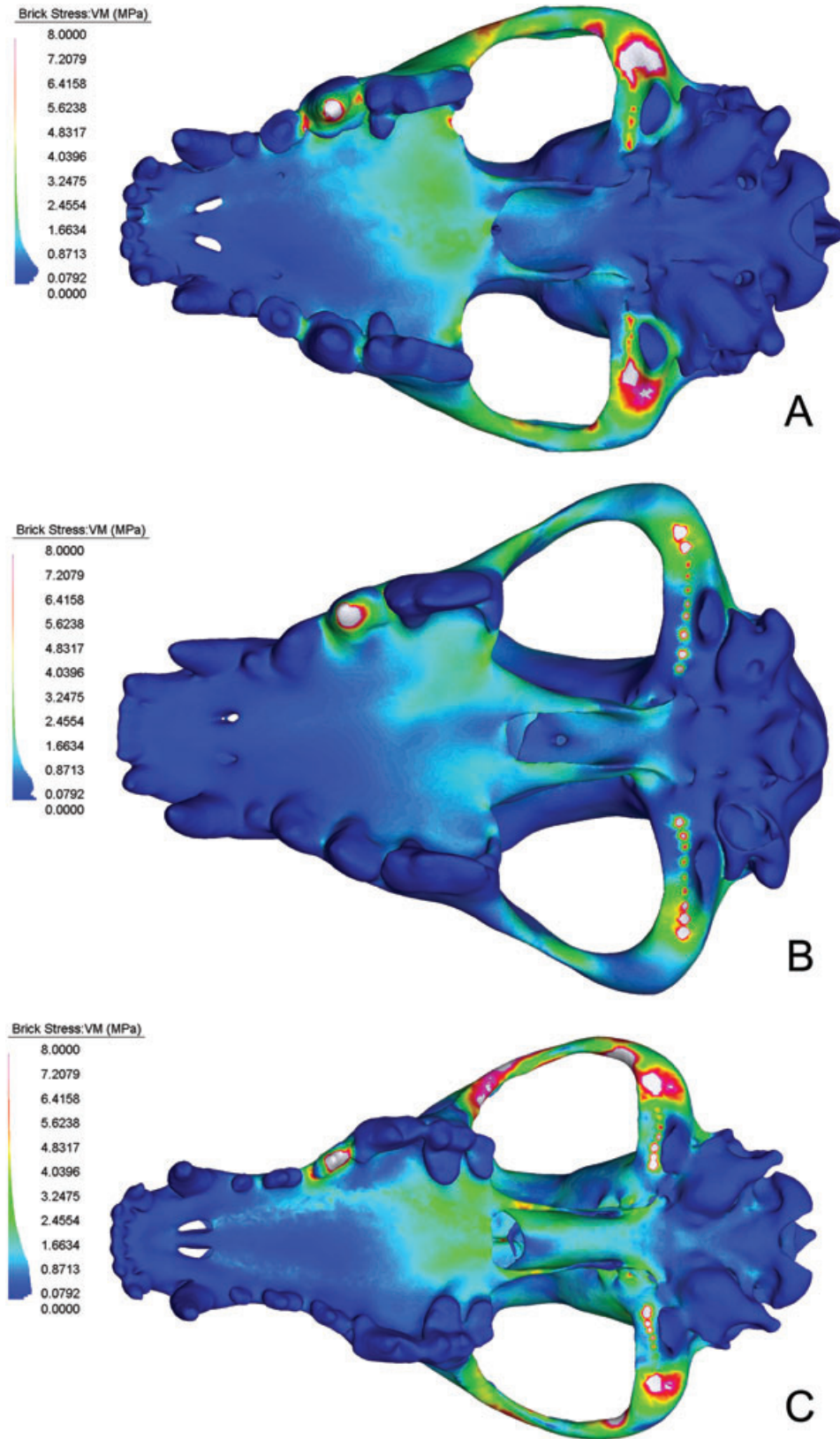


Figure 3. Ventral views of Von Mises (VM) stress distribution during left P3-biting scenario in the cranium of (A) *Crocuta crocuta*, (B) *Dinocrocuta gigantea*, and (C) *Canis lupus*. Legends are as shown in Fig. 2.

Table 4. Comparative statistics of Von Mises stress in the finite element models of the *Crocota crocuta*, *Dinocrocota gigantea*, and *Canis lupus* skulls

	<i>Crocota crocuta</i>	<i>Dinocrocota gigantea</i>	<i>Canis lupus</i>
Entire model			
Median scaled \pm SE (MPa)	0.4074 \pm 0.0019	0.4715 \pm 0.0016	0.5440 \pm 0.0019
Scaled MAD (MPa)	0.35	0.41	0.45
Scaled IQR (MPa)	1.21	1.24	1.28
Frontal dome			
Median scaled \pm SE (MPa)	0.6950 \pm 0.0132	0.7033 \pm 0.0154	1.2075 \pm 0.0220
Scaled MAD (MPa)	0.48	0.5	0.78
Scaled IQR (MPa)	1.25	1.18	1.79
Maximum scaled (MPa)	57.77	6.27	18.33

The comparative data are for left P3 unilateral biting. Abbreviations are as shown in Table 1. For a definition of the descriptive statistics, see text.

Table 5. Comparative statistics of Von Mises stress in the finite element models of the *Crocota crocuta*, *Dinocrocota gigantea*, and *Canis lupus* skulls

	<i>Crocota crocuta</i>	<i>Dinocrocota gigantea</i>	<i>Canis lupus</i>
Entire model			
Median scaled \pm SE (MPa)	0.3951 \pm 0.0018	0.4519 \pm 0.0015	0.4872 \pm 0.0017
Scaled MAD (MPa)	0.33	0.39	0.41
Scaled IQR (MPa)	1.11	1.17	1.17
Frontal dome			
Median scaled \pm SE (MPa)	0.6083 \pm 0.0113	0.6141 \pm 0.0133	1.1824 \pm 0.0228
Scaled MAD (MPa)	0.41	0.43	0.77
Scaled IQR (MPa)	1.07	1.02	1.86
Maximum scaled (MPa)	52.76	6.74	20.45

The comparative data are for left P4 unilateral biting. Abbreviations are as shown in Table 1. For a definition of the descriptive statistics, see text.

similar stress reactions in all three models, in addition to M1 biting in the *Canis* model. Although the more posteriorly placed teeth have more mechanical advantage by leverage, the differences in stress distribution that might represent adaptations to specific biting regimes (e.g. P3 bone cracking) are not obvious from the analyses. Thus, the crania of the three carnivorans investigated in the present study cannot be said to have functional advantages for any particular biting scenario tested. It could be that the teeth are simply too close in proximity for the analyses to detect differences in performance (e.g. larger differences in stress magnitude and distribution are to be expected for P4 versus canine biting in all cases by the principle of lever mechanics). Another likely explanation could be that the cranium, a product of complex selective pressure for different functions (e.g. protection of brain, tuning of sensory organs, bite force, gape, variation in dental function across tooth row), would not appear optimized for specifically P3

bone-cracking, even if it represents a mechanically demanding task.

CANIS LUPUS

In the *Canis* model, the median scaled stress of the interorbital region was more than double that of the entire cranium. In part, this could be interpreted as the poor ability of the inter-orbital region to dissipate stress in *Canis*. What was unexpected, again, is that this doubling of median stress is observed for all three biting cases. One might expect the inter-orbital region to respond differently when biting with the slender P3 versus biting with the carnassial or the bone-crushing M1. By visually checking for artificial sharp features and highly distorted triangular elements using error-checking functions in the STRAND7 Finite element software, it was concluded that no major errors ensued during the creation of the finite element model; thus, it is unlikely that some critical error in

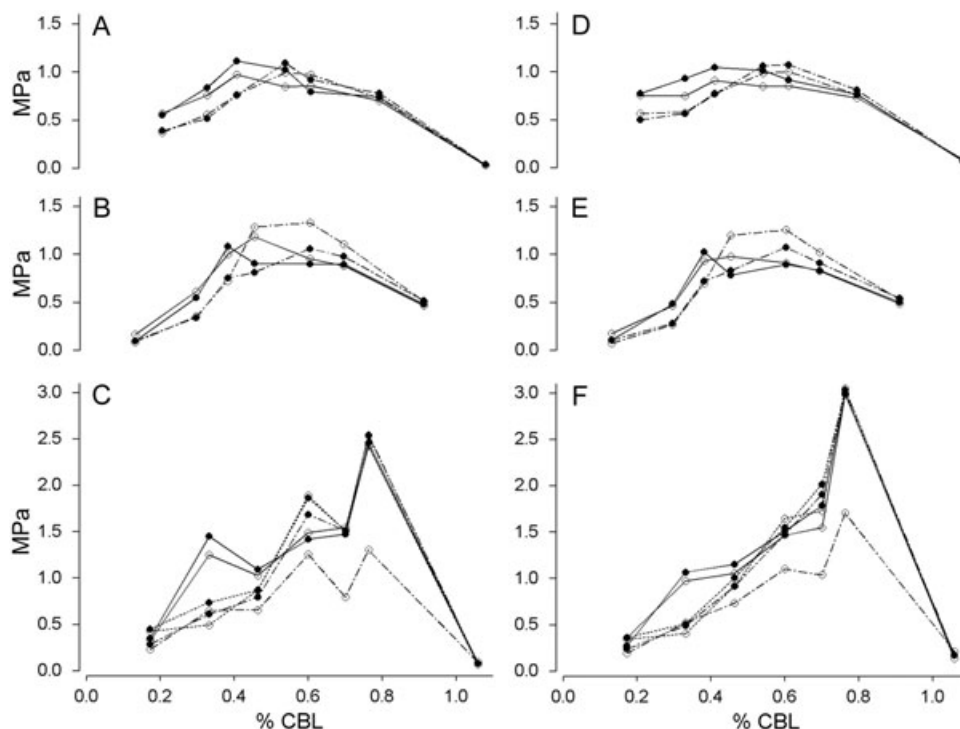


Figure 4. Von Mises stress gradients from the anterior to posterior cranium along the mid-sagittal plane in analogous anatomical sampling points. Stresses from single node samples of (A) *Crocuta crocuta*, (B) *Dinocrocuta gigantea*, and (C) *Canis lupus* and mean stresses from node group samples of (D) *Crocuta crocuta*, (E) *Dinocrocuta gigantea*, and (F) *Canis lupus* are shown. The data points (from left to right) represent stress recorded along the mid-sagittal plane in lateral alignment with (1) anterior border of nasal bones, (2) infraorbital foramina, (3) anterior boundary of the orbits, (4) the inter-orbital region between the post-orbital processes, (5) post-orbital restriction of the frontal-parietal region, (6) anterior-most point of the sagittal crest, and (7) posterior-most point of the sagittal crest. The points are plotted as percentages of skull condylobasal length (CBL) in the anterior–posterior direction. Left side, filled symbol; right side, open symbol; P3 biting, solid line; P4 biting, dashed line; M1 biting, dotted line.

modelling caused this pattern. Canine bite force estimations based on the dry skull method suggest that *Canis lupus* has a higher bite strength than *Crocuta crocuta* (Wroe *et al.*, 2005). In that study, however, it was also suggested that bite strength does not necessarily imply bone-cracking, which might be more closely associated with structural adaptations in teeth and cranial bones. The findings from the present study suggest structural adaptation in the cranium of the bone cracking *Crocuta* compared to *Canis* for the scenarios tested. The high stress observed in the dorsal cranium of *Canis* is in accordance with the suggestion of Wroe *et al.* (2005) who demonstrated that larger theoretical bite forces in *Canis* are not necessarily realized because of cranial structure constraints to bone-cracking, in addition to any structural improvement in teeth.

An important point to be noted is that, given the differences in cranial morphology and masticatory muscle attachment sites, the skull of *Canis* required the highest muscle input to produce the same bite

force compared to the other two models (see Appendix, Table A1). The high input force is probably what created the elevated stresses observed throughout the *Canis* model. Furthermore, upon examining the regions of highest stress in all three models, it was found that the ends of the zygomatic arches generally exhibit relatively high stress values (Figs 2, 3). The presence of these high stresses are also likely to be partially attributed to muscle force action because the downward pull of the masseter muscles would tend to bend the arches in the ventro-medial direction. Furthermore, the models constructed in the present study do not contain any sutures, which have been shown to represent sites of high strain and may be important in stress distribution across cranial bones (Herring & Teng, 2000).

CROCUTA AND DINOCROCUTA

Discussions of correlation between craniodental form and performance in hyaenids have often highlighted

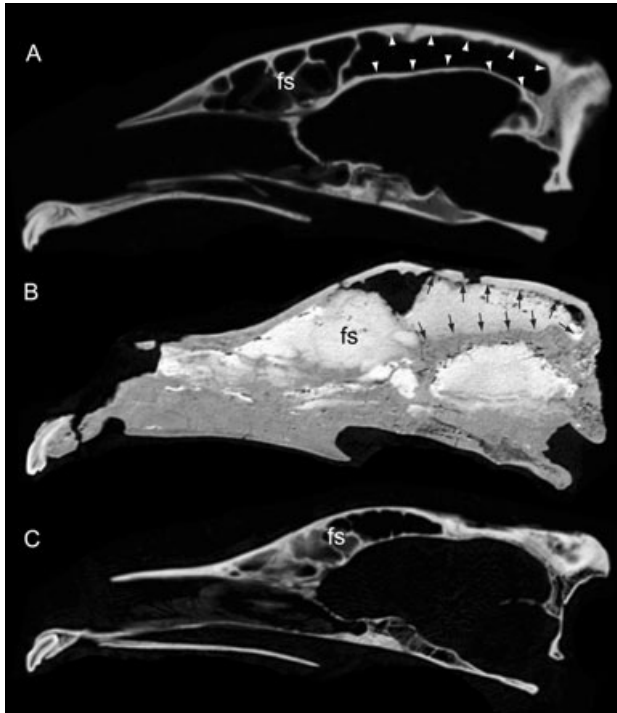


Figure 5. Computer tomography images of (A) *Crocuta crocuta*, (B) *Dinocrocuta gigantea*, and (C) *Canis lupus* taken as lateral views of the mid-sagittal section of the cranium. The frontal sinus (fs) is indicated in all three crania, and caudal expansion of the frontal sinus in *C. crocuta* and *D. gigantea* is noted by arrows. The internal cavities of the *D. gigantea* specimen are filled with matrix, which is light grey in colour in the frontal sinus area. All crania are scaled in the figure to the same approximate length.

the caudally extended frontal sinus present in members of the group. The extent of the development of the posterior frontal sinus in hyaenids is unique among carnivorans (Joeckel, 1998), and functional relevance to stress dissipation during bone cracking has been speculated (Werdelin, 1989). More recently, it was shown, through examination of theoretical morphology, that Joeckel's (1998) hypothesis appears to hold, at least for *C. crocuta* (J. Tanner, pers. comm.). In the *Crocuta* model, the thin bones delineating the frontal sinus are preserved and included; however, the *Dinocrocuta* model has a single, continuous cavity inside the cranium. A caudally extended frontal sinus is definitely present in *Dinocrocuta*, but too poorly preserved to be included in the model (Fig. 5). Furthermore, the hypothesis of Joeckel (1998) places functional significance on the formation of a shell-like forehead by the presence of caudally elongate frontal sinus, and not the presence of the sinus *per se*. Even though the bony plate between the frontal sinus and brain cavity is incompletely pre-

served in *Dinocrocuta*, it is not expected to be load-bearing because of its contact with the brain roof in life. Thus, if the enlargement of the sinus is causal in creating the frontal dome of the bone-cracking carnivorans, it could explain the similarity in stress distribution between *Dinocrocuta* and *Crocuta*. The presence of frontal sinus structure in the *Crocuta* model, however, created regions of concentrated stress in the bony struts surrounding the sinus. The curvature is acute in some of the bony struts; thus, stress does not conduct smoothly through the area. A contributing factor to this result could be the lack of soft tissue in the models. The frontal sinus of the domestic dog has been shown to contain a covering of respiratory epithelium (Reznik, 1990; Craven *et al.*, 2007) in the same region where the *Crocuta* model has concentrated stress (Fig. 5). A dissection of the cranium of *H. hyaena* (LACM freezer catalogue number 42 206) confirmed the presence of this epithelium throughout the frontal sinus of that hyaenid. Although the material properties of the respiratory epithelium are not known, its close association with the inner surface of the frontal sinus might nevertheless impart a certain degree of structural continuum across which stress could be distributed. Further testing with incorporation of soft tissue material into the model is needed to clarify whether the dissipation of stress occurs in those small regions.

MID-SAGITTAL POINT-SAMPLING STRESS

Clearer patterns arise when the mid-sagittal point-sampling data are graphed across biting scenarios for each model (Fig. 4A, B, C). Both *Crocuta* and *Dinocrocuta* show a much smoother increase in stress just caudal of the nasal opening and extending to the sagittal crest. The down-sloping stress values caudal of the biting point in *Crocuta* supports the hypothesis that the curvature of the cranium matches the path of stress distribution to function in dissipation (Fig. 4A). A similar pattern is observed in *Dinocrocuta*; however, it is less clear, with peaks distributed between the anterior orbital border and the post-orbital constriction (Fig. 4B). In general, both the *Dinocrocuta* and *Crocuta* models demonstrate gradual change in stress levels across the dorsal cranium, approximately matching the shape of the frontal dome in their stress distribution patterns. By stark contrast, point sampling of the *Canis* model shows multiple stress peaks across different scenarios along the mid-sagittal plane. The anterior stress peaks demonstrate that the *Canis* cranium is not as suited for P3 biting as *Crocuta* or *Dinocrocuta* (Fig. 4, Table 4). A peak in stress could be better buffered by the cranium if it can be transmitted caudally to the active temporalis muscles that are undergoing

tension during biting (Buckland-Wright, 1978). The interpretation appears to stand for both the *Dinocrocuta* and *Crocuta* models, and may explain the very low stresses in the region of temporalis muscle action (Fig. 2).

Mid-sagittal sampling of P4 biting in *Canis* returned much lower stresses using the right P4 than the left (Fig. 4C, F); re-examination of the results indicate that the heightened stress in left P4 biting is not concentrated in small regions but, instead, is a general elevation of stress across the entire cranium. The same models were used for the P3 and M1 scenarios as well, which did not return such asymmetry. It is unclear why this difference exists; however, other than the magnitude, the general trend of the stress peaks remains valid for all analyses, and does not affect the interpretation made here. Single node stress gradients in the *Canis* model are congruent with theoretical expectation (Fig. 4C). The stress gradient along the mid-sagittal plane of the *Canis* model matches the basic pattern of bending stress calculation from a beam model of a dry *Canis* skull (Thomason, 1991): there is a small peak in the region above the infraorbital foramina on the mid-sagittal plane. The second, higher peak occurs near the region between the post-orbital processes. No data were shown for the posterior cranium by Thomason (1991). Although the absolute magnitude of stress is higher in Thomason's calculations, it is of a different biting scheme compared to the present study (i.e. canine biting instead of P3-M1 biting). This lends additional support to the models, and also that the analyses demonstrate the relatively less well 'designed' cranium of the *Canis* compared to the other two models for the biting scenarios tested (Tables 4, 5). With the added advantage of zig-zag Hunter-Schreger enamel banding (Rensberger & Stefen, 2006), which is not present in *C. lupus* (Stefen, 1999), the robust craniodental morphology of *Dinocrocuta* is thus likely to be both capable and functional for bone cracking.

An interesting pattern is revealed when single node stress is compared with mean stress over a 6-mm diameter area in the point-sampling analysis. Whereas the stress patterns for *Crocuta* and *Dinocrocuta* remain unchanged between the two sampling methods (Fig. 4A, B, D, E), the same cannot be said for *Canis*. In *Canis*, a steep slope is still present leading posteriorly to the anterior border of the sagittal crest, but the mean stresses of nodes around a larger area at each landmark appear much smoother than the single node stresses (Fig. 4C, F). This could be explained by the presence of sharper stress gradients in those regions in the *Canis* model compared to the other two models, thereby allowing single node sampling to pick up local extremes. In both *Crocuta*

and *Dinocrocuta*, the increase in stress from the lateral sides toward the mid-sagittal plan is visibly more gradual (Fig. 2A, B), whereas, in the *Canis* model, small patches of higher stress appear more abruptly (Fig. 2C). Stresses collected from a group of nodes around a landmark would thus tend to average out small areas of high stress. These findings further suggest that the *Canis* skull model experiences not only elevated stress along the entire mid-sagittal plane relative to the *Crocuta* and *Dinocrocuta* models (Tables 1–3), but also shows steep and unevenly distributed stress gradients in the nasal and interorbital region. These results provide potential avenues for validation and testing with *in vivo* strain gauge experiments (Herring *et al.*, 2001), which may help to explain additional nuances in the differences between *Crocuta* and *Canis* observed here.

BROADER IMPLICATIONS AND FUTURE DIRECTIONS

The *Dinocrocuta* cranium represents an individual with unworn permanent dentition and incompletely developed sagittal crest and frontal dome. As the finite element model of *Dinocrocuta* was made from a relatively young individual, the patterns observed here might be affected by ontogeny. From observations made on specimens of more mature individuals, the shape of the forehead becomes much more pronounced and 'vaulted', and may have been better aligned with vertically oriented stress, thereby channeling them dorsoposteriorly. *Crocuta*, on the other hand, shows relatively less modification of the frontal shape through ontogeny. The smooth curvature in *Crocuta* thus might persist throughout growth, altering the stress distribution curve to a lesser degree than in *Dinocrocuta* (Fig. 4A, B).

Much previous theoretical work has been conducted on the mechanics of the mammalian mandibles (Greaves, 1982, 1983, 1985, 2000), which firmly established the 'one third rule'. The rule provides that, given all considerations to maximize bite force, function, and mechanical stability, the resultant muscle force vector from the action of masticatory muscles fall 30% of the way along the jaw length away from the jaw joint. To maintain stability and prevent frequent torsional loading in the temporomandibular joint, no biting should occur within 30% of the length from the jaw joint. In addition, the proper occlusion required for the shearing carnassials (upper P4 and lower m1) places an evolutionary constraint on the location of those teeth and in turn the arrangement of other cheek teeth relative to them (Savage, 1977). These are factors that might explain the number, position, as well as the use of cheek teeth in *Dinocrocuta*. From attrition patterns of tooth cusps observed in a sample of eight *D. gigantea* skulls from Gansu

Province, China, it can be concluded that all cheek teeth are used and worn, just as in extant spotted hyenas. Thus, the cranium must respond to the overall biting function over evolutionary time, and not just to the tooth doing the maximum amount of work (i.e. P3 bone cracking). This again would explain why there is little difference between biting scenarios within the premolar tooththrow.

The finite element approach has great potential in reconstructing past ecomorphology by testing anatomically inferred form–function relationships (Rayfield, 2007). More specifically, the comparison of living and fossil taxa using this technique holds promises for testing current functional hypotheses and refining ecomorphological definitions. For example, subtleties in cranial mechanics of carnivorans (e.g. borophagine canids, amphicyonids) and creodonts (e.g. hyaenodontids) that are inferred bone-crackers could be elucidated in this manner by comparison to their closest living relatives (e.g. caniform carnivorans) and with living bone-crackers (i.e. *Crocuta crocuta*). On the other hand, the undifferentiated cranial response to premolar bites tested in the present study highlights difficulties in identifying bone-cracking adaptations when the cranium might be more generally adapted as a result of multiple evolutionary constraints. Thus, the application of finite element analysis could be further refined to test new evolutionary questions that stem from each additional analysis. Among the anticipated developments: (1) more rigorous statistical testing techniques for analysing finite element stress and strain data; (2) a more fundamental understanding of ecomorphology by finite element analyses of wide-ranging theoretical morphologies; and (3) the application of comparative finite element analysis to an entire clade of closely related species to examine function in a phylogenetic context, will all continue to improve the utility of the finite element method in our understanding of functional morphology evolution.

CONCLUSION

Analyses using three finite element models showed that the crania of *C. crocuta* and *D. gigantea* experienced lower stress for the same P3 and P4 biting scenarios using identical bite force than *C. lupus*. Differences in biting scenarios were small within each model and the same holds true for stress dissipation in the frontal region. Of the bone cracking carnivorans, *Dinocrocuta* experienced lower overall stress in the inter-orbital region as well as lower maximum stress. Point sampling of stresses along the mid-sagittal plane of the models demonstrate the ability of *Dinocrocuta* and *Crocuta* crania in smoothly conducting stress into the inter-orbital region, probably allowing the stress to be dissipated through the

shell-like dorsal cranium and/or tension in the temporalis muscles. This is in stark contrast to the multiple peaks of stress in the *Canis* model, which does not spread stress evenly. Through the examination of functional morphology using finite element analysis, the present study demonstrates that the morphology of the frontal region plays an important role in conducting stress, regardless of premolar usage. The actual capability of a bone-cracking individual may be balanced by a continuous shift in dental and cranial mechanical advantage and requirements during its ontogeny. The examination of purported bone-cracking taxa in other mammalian lineages would shed light on the extent of functional similarity that underlies morphological convergence.

ACKNOWLEDGEMENTS

I thank Xiaoming Wang and Gary Takeuchi of LACM for discussion, guidance and encouragement; Betsy Dumont, Sean Werle, and Ian Grosse for training and hospitality during the Finite Element Analysis in Biology workshop in June 2007 at the University of Massachusetts, Amherst; Betsy Dumont and Ian Grosse for access to their BONELOAD program for modelling jaw musculature in the skull models; Michael McNitt-Gray at UCLA Medical Center for CT scanning the specimens; Graham Slater at UCLA for discussion and access to software; the editor and referees for their dedicated reading of the manuscript and stimulating ideas that greatly improved the content of this paper; Jim Dines at LACM for extant specimen loans; Zhanxiang Qiu at the Institute of Vertebrate Paleontology and Paleoanthropology in Beijing, China for an extended loan of the *Dinocrocuta gigantea* skull; Jill McNitt-Gray, Reyes Enciso, Henryk Flashner, and Faizal Kamaruddin at the University of Southern California (USC) for comments and help with software programs; and the Dinosaur Institute at LACM for research space. This research was funded by a USC Zumberge grant, American Society of Mammalogists grant-in-aid of research, a National Science Foundation Graduate Research Fellowship and National Science Foundation of China (40730210).

REFERENCES

- Binder WJ, Van Valkenburgh B. 2000.** Development of bite strength and feeding behaviour in juvenile spotted hyenas (*Crocuta crocuta*). *Journal of the Zoological Society of London* **252**: 273–283.
- Buckland-Wright JC. 1978.** Bone structure and the patterns of force transmission in the cat skull (*Felis catus*). *Journal of Morphology* **155**: 35–62.
- Cowin SC. 1989.** The mechanical properties of cortical bone tissue. In: Cowin SC, ed. *Bone mechanics*. Boca Baton, FL: CRC Press, 97–127.

- Craven BA, Neuberger T, Paterson EG, Webb AG, Josephson EM, Morrison EE, Settles GS. 2007.** Reconstruction and morphometric analysis of the nasal airway of the dog (*Canis familiaris*) and implications regarding olfactory airflow. *The Anatomical Record* **290**: 1325–1340.
- Dessem D. 1989.** Interactions between jaw-muscle recruitment and jaw-joint forces in *Canis familiaris*. *Journal of Anatomy* **164**: 101–121.
- Dumont ER, Piccirillo J, Grosse IR. 2005.** Finite-element analysis of biting behavior and bone stress in the facial skeletons of bats. *The Anatomical Record Part A* **283A**: 319–330.
- Erickson GM, Catanese J III, Keaveny, TM. 2002.** Evolution of the biomechanical material properties of the femur. *The Anatomical Record* **268**: 115–124.
- Erxleben JCP. 1777.** *Systema regni animalis, Classis I, Mammalia*. Lipsiae.
- Ferretti MP. 2007.** Evolution of bone-cracking adaptations in hyaenids (Mammalia, Carnivora). *Swiss Journal of Geoscience* **100**: 1–12.
- Gorniak GC, Gans C. 1980.** Quantitative assay of electromyograms during mastication in domestic cats (*Felis catus*). *Journal of Morphology* **163**: 253–281.
- Greaves WS. 1982.** A mechanical limitation on the position of the jaw muscles of mammals the one-third rule. *Journal of Mammalogy* **63**: 261–266.
- Greaves WS. 1983.** A functional analysis of carnassial biting. *Biological Journal of the Linnean Society* **20**: 353–364.
- Greaves WS. 1985.** The generalized carnivore jaw. *Zoological Journal of the Linnean Society* **85**: 267–274.
- Greaves WS. 2000.** Location of the vector of jaw muscle force in mammals. *Journal of Morphology* **243**: 293–299.
- Grosse I, Dumont ER, Coletta C, Tolleson A. 2007.** Techniques for modeling muscle-induced forces in finite element models of skeletal structures. *The Anatomical Record* **290**: 1069–1088.
- Herring SW, Rafferty KL, Liu ZJ, Marshall CD. 2001.** Jaw muscles and the skull in mammals: the biomechanics of mastication. *Comparative Biochemistry and Physiology Part A* **131**: 207–219.
- Herring SW, Teng S. 2000.** Strain in the braincase and its suture during function. *American Journal of Physical Anthropology* **112**: 575–593.
- Irons B, Ahmad S. 1980.** *Techniques of finite elements*. New York, NY: John Wiley & Sons.
- Joeckel RM. 1998.** Unique frontal sinuses in fossil and living Hyaenidae (Mammalian, Carnivora): description and interpretation. *Journal of Vertebrate Paleontology* **18**: 627–639.
- Laitman JT. 2005.** A microscope on vertebrate form and function: the power of finite element analysis. *The Anatomical Record Part A* **283A**: 251–252.
- Linnaeus C. 1758.** *Systema naturae per regna tria naturae, secundum classes, ordines, genera, species, cum characteribus, differentiis, synonymis, locis. Vol. 1: Regnum animale. Editio decima, 1758 (12th edition of Linnaeus 1758)*. Stockholm: Societatis Zoologicae Germanicae.
- McHenry C, Wroe S, Clausen PD, Moreno K, Cunningham E. 2007.** Supermodeled sabercat, predatory behavior in *Smilodon fatalis* revealed by high-resolution 3D computer simulation. *Proceedings of the National Academy of Sciences of the United States of America* **104**: 16010–16015.
- Nowak RM. 1999.** *Walker's carnivores of the world*. Baltimore, MD: The Johns Hopkins University Press.
- Peterson J, Dechow PC. 2003.** Material properties of the human cranial vault and zygoma. *The Anatomical Record Part A* **274A**: 785–797.
- Peterson J, Wang Q, Dechow PC. 2006.** Material properties of the dentate maxilla. *The Anatomical Record Part A* **288A**: 962–972.
- Pidaparti RM, Vogt A. 2002.** Experimental investigation of Poisson's ratio as a damage parameter for bone fatigue. *Journal of Biomedical Materials Research* **59**: 282–287.
- Rasband WS. 1997–2007.** *ImageJ*. Bethesda, MD: National Institutes of Health.
- Rayfield EJ. 2004.** Cranial mechanics and feeding in *Tyrannosaurus rex*. *Proceedings of the Royal Society of London Series B, Biological Sciences* **271**: 1451–1459.
- Rayfield EJ. 2007.** Finite element analysis and understanding the biomechanics and evolution of living and fossil organisms. *Annual Review of Earth and Planetary Science* **35**: 541–576.
- Rayfield EJ, Norman DB, Jorner CC, Horner JR, Smith PM, Thomason JJ, Upchurch P. 2001.** Cranial design and function in a large theropod dinosaur. *Nature* **409**: 1033–1037.
- Reilly DT, Burstein AH. 1975.** The elastic and ultimate properties of compact bone tissue. *Journal of Biomechanics* **8**: 393–405.
- Rensberger JM. 1995.** Determination of stresses in mammalian dental enamel and their relevance to the interpretation of feeding behaviors in extinct taxa. In: Thomason JJ, ed. *Functional morphology in vertebrate paleontology*. New York, NY: Cambridge University Press, 151–172.
- Rensberger JM, Stefen C. 2006.** Functional differentiations of the microstructure in the upper carnassial enamel of the spotted hyena. *Palaeontographica Abt. A* **278**: 149–162.
- Reznik GK. 1990.** Comparative anatomy, physiology, and function of the upper respiratory tract. *Environmental Health Perspectives* **85**: 171–176.
- Richmond BG, Wright BW, Grosse I, Dechow PC, Ross CF, Spencer MA, Strait DS. 2005.** Finite element analysis in functional morphology. *The Anatomical Record Part A* **283A**: 259–274.
- Ross CF. 2005.** Finite element analysis in vertebrate biomechanics. *The Anatomical Record Part A* **283A**: 253–258.
- Savage RJ. 1977.** Evolution in carnivorous mammals. *Palaeontology* **20**: 237–271.
- Schlosser M. 1903.** Die fossilen Säugethiere Chinas nebst einer Odontographie der recenten Antilopen. *Abhandlungen königlich bayerischen Akademie Wissenschaften* **22**: 1–221.
- Shahar R, Zaslansky P, Barak M, Friesem AA, Currey JD, Weiner S. 2007.** Anisotropic Poisson's ratio and compression modulus of cortical bone determined by speckle interferometry. *Journal of Biomechanics* **40**: 252–264.
- Stefen C. 1999.** Enamel microstructure of recent and fossil

- Canidae (Carnivora: Mammalia). *Journal of Vertebrate Paleontology* **19**: 576–587.
- Stefen C, Rensberger JM. 2002.** The specialized enamel structure of hyaenids (Mammalia, Hyaenidae): description and development within the lineage – including percutids. *Zoologische Abhandlungen* **52**: 127–147.
- Thomason JJ. 1991.** Cranial strength in relation to estimate biting forces in some mammals. *Canadian Journal of Zoology* **69**: 2326–2333.
- Van Valkenburgh B. 1988.** Trophic diversity in past and present guilds of large predatory mammals. *Paleobiology* **14**: 155–173.
- Van Valkenburgh B. 1989.** Carnivore dental adaptations and diet: a study of trophic diversity within guilds. In: Gittleman JL, ed. *Carnivore behavior, ecology, and evolution*. New York, NY: Cornell University Press, 410–436.
- Van Valkenburgh B. 1990.** Skeletal and dental predictors of body mass in carnivores. In: Damuth J, MacFadden BJ, eds. *Body Size in mammalian paleobiology: estimation and biological implications*. Cambridge: Cambridge University Press, 181–205.
- Van Valkenburgh B. 1999.** Major patterns in the history of carnivorous mammals. *Annual Review of Earth and Planetary Science* **27**: 463–493.
- Van Valkenburgh B. 2001.** Chapter 5. The dog-eat-dog world of carnivores: a review of past and present carnivore community dynamics. In: Stanford CB, Bunn HT, eds. *Meat eating and hominid evolution*. Oxford: Oxford Press, 101–121.
- Wang Q, Strait DS, Dechow PC. 2006.** A comparison of cortical elastic properties in the craniofacial skeletons of three primate species and its relevance to the study of human evolution. *Journal of Human Evolution* **51**: 375–382.
- Werdelin L. 1989.** Constraint and adaptation in the bone-cracking canid *Osteoborus* (Mammalia: Canidae). *Paleobiology* **15**: 387–401.
- Werdelin L. 1996.** Chapter 17. Carnivoran ecomorphology: a phylogenetic perspective. In: Gittleman JL, ed. *Carnivore behavior, ecology, and evolution*. New York, NY: Cornell University Press, 582–624.
- Wroe S, McHenry C, Thomason JJ. 2005.** Bite club: comparative bite force in big biting mammals and the prediction of predatory behaviour in fossil taxa. *Proceedings of the Royal Society of London Series B, Biological Sciences* **272**: 619–625.

APPENDIX

SUMMARY OF THE THREE FINITE ELEMENT MODELS ANALYSED IN THE PRESENT STUDY

The muscle cross-sectional areas were measured from posterodorsal and ventral view photos as in Thomason (1991). Balancing muscles were given 60% of the magnitude of working muscle forces. The frontal dome region was identified by a section of similar volume between the post-orbital processes of the three models.

Table A1. Finite element model parameters of the three skulls studied.

	<i>Dinocrocuta</i>	<i>Crocuta</i>	<i>Canis</i>
Body mass (kg)*	199.53	36.31	46.24
(Species body mass range; kg)†	–	40–86	18–80
Model condylobasal length (mm)	198.15	209.91	275.66
(Actual condylobasal length; mm)	322.36	213.76	244.90
Model maximum width (mm)	147.40	137.45	163.58
(Actual maximum width; mm)	251.72	139.56	142.66
4-noded tetrahedral elements	1 532 146	973 734	1 120 780
Total element volume (mm ³)	324 610.7	326 625.0	324 513.3
Model skull mass (g)‡	649.22	653.25	649.03
(Actual dry skull mass; g)	–	477.85	335.50
Temporalis cross-section (mm ²)	6.28×10^3	2.42×10^3	3.81×10^3
Masseter cross-section (mm ²)	5.67×10^3	1.90×10^3	2.93×10^3
Temporalis contribution (%)	52.54	55.92	56.56
Masseter contribution (%)	47.46	44.08	43.44
Modelled bite force (N)	318.15	318.15	318.15
Required muscle force (N)	1 095.55	1 376.36	1 537.92
Total muscle plate area (mm ²)	1.13×10^4	1.36×10^4	5.51×10^4
Balancing temporalis (N)	215.46	288.62	326.19
Balancing masseter (N)	194.62	227.51	250.53
Working temporalis (N)	359.10	481.04	543.65
Working masseter (N)	324.37	379.19	417.54
Frontal dome elements	14 432	22 043	16 391
Frontal dome volume (mm ³)	4.40×10^3	4.43×10^3	4.59×10^3

*Estimated from condylobasal length using regression equations for > 100 kg (*Dinocrocuta*) and 10–100 kg (*Crocuta* and *Canis*) categories in Van Valkenburgh (1990).

†Nowak (1999).

‡Estimated using dog femur cortical bone density of 2 mg mm⁻³ (Cowin, 1989).